

Processing-Dependent Microstructure of AgCl–CsAgCl₂ Eutectic Photonic Crystals

Jaewon Choi, Ashish A. Kulkarni, Erik Hanson, Daniel Bacon-Brown, Katsuyo Thornton, and Paul V. Braun*

Directional solidification of a eutectic melt allows control over the resultant eutectic microstructure, which in turn impacts both the mechanical and optical properties of the material. These self-organized phase-separated eutectic materials can be tuned to have periodicities from tens of micrometers down to nanometers. Furthermore, the two phases possess differences in their refractive index leading to interesting optical properties that can be tailored within the visible to infrared wavelength regime. It is found the binary salt eutectic AgCl–CsAgCl₂ system forms a rod microstructure with sample draw rates up to 0.2 mm s⁻¹ which transitions to a lamellar microstructure at draw rates greater than 0.36 mm s⁻¹. Heat-transfer simulations reveal a draw rate-dependent direction of motion of the solidification front, which for a range of draw rates requires nucleation of the minority solid phase at the sample wall. Phase-field modeling indicates that the initial eutectic structure at the sample boundary, either rod or lamellar, dictates the bulk eutectic morphology. These samples contain submicrometer periodicities which coupled with their optical transparency results in them exhibiting draw rate-dependent near-IR reflectance peaks consistent with stop bands for 2D hexagonal (rod) and 1D planar (lamellar) photonic crystals.

with large refractive index contrasts and varied structural motifs have been successfully fabricated from a wide range of materials.^[7,8] However, top-down (e.g., lithographic) formation of large volumes of photonic crystals is a challenge. Self-organization techniques, such as eutectic solidification, have been shown as a possible path to forming large volumes of photonic crystals.^[9–14] Among possible motifs provided by eutectic solidification, the regular microstructures of lamellar and rod eutectics have direct resemblance to 1D and 2D photonic crystals, respectively, where the phase-separated components provide the required contrast in the refractive index to exhibit a unique optical response.^[6] The components of eutectic materials can be chosen from metals, semiconductors, polymers, organics, ceramics, or salts; thus providing metal, dielectric, or even metallodielectric composites with which to synthesize (or to act as templates for) photonic crystals.^[11,13,15–23] Recent

1. Introduction


Directional solidification of eutectic materials results in self-organized phase-separated micro- and nanostructures whose periodicities can be tuned to be on the order of visible or infrared wavelengths of light.^[1–5] If the microstructure is highly ordered and the phases have different optical properties, the material may exhibit strong diffraction of light with wavelengths comparable to the characteristic dimension of the structure; these structures are termed as photonic crystals.^[6] Photonic crystals

examples from literature have demonstrated the formation of photonic crystals and other optically interesting structures (for applications like diffraction gratings, phase-separated scintillators with light guiding, and absorption-induced transparency) in directionally solidified chloride-based molten salt eutectics, such as AgCl–KCl,^[16,18,22] NaCl–CsI,^[23,24] CuI–KCl,^[15] and KCl–LiF.^[25] The eutectic solidification-based synthesis route is particularly simple if the eutectics have a low melting temperature and low surface energy, are devoid of any corroding components, like fluorides, and do not require controlled atmospheres during fabrication. However, even without these ideal factors, eutectic solidification is a quite well-established industrial process, and many challenging chemistries can be directionally solidified.

The binary salt eutectic AgCl–CsAgCl₂ has the advantageous properties of a eutectic temperature (258 °C) and surface energy (135 mJ m⁻²) at its eutectic temperature lower than most other eutectic salt systems, but it has received only minimal attention.^[26–28] Here, we show that when directionally solidified, AgCl–CsAgCl₂ has a tendency to form either a rod structure or lamellar structure depending on the directional solidification draw rates. While not unprecedented, as some binary metal eutectics, e.g., Al–Al₄Ca,^[29] Au–Co,^[30] Cd–Sn,^[31] Ni–W,^[32] Ag–Cu,^[33] and Al–Cu,^[34] have been known to show transitions

Dr. J. Choi, A. A. Kulkarni, D. Bacon-Brown, Prof. P. V. Braun
Department of Materials Science and Engineering
Frederick Seitz Materials Research Laboratory
Beckman Institute for Advanced Science and Technology
University of Illinois at Urbana-Champaign
Urbana, IL 61801, USA
E-mail: pbraun@illinois.edu

E. Hanson, Prof. K. Thornton
Department of Materials Science and Engineering
University of Michigan
Ann Arbor, MI 48109, USA

 The ORCID identification number(s) for the author(s) of this article can be found under <https://doi.org/10.1002/adom.201701316>.

DOI: 10.1002/adom.201701316

from rod to lamellar structure, to our knowledge no other salt eutectics have been shown to exhibit this property. In general, this rod to lamellar transition can be influenced by either volume fraction, entropy of solution of the constituent solid solution phases, interfacial boundary energy anisotropy, or the growth rate, depending on the material system.^[4,33,35,36] The rod to lamellar microstructure transition is powerful in that it can be utilized to obtain a diversity of optical properties from a single material, using the processing conditions alone as the tuning knob. Specifically, the material can be interchangeably rendered into 1D and 2D photonic crystals.^[6] Although the photonic properties of lamellar eutectic salts have previously been studied, that is, as a 1D photonic crystal, the optical properties of rod 2D photonic crystal eutectic microstructures have not been investigated. Here, we utilize the microstructural transition of the AgCl-CsAgCl₂ salt eutectic system and employ a combined experimental and simulation approach to understand the processing-dependent microstructural formation and resultant optical properties.

2. Results and Discussion

The AgCl-CsAgCl₂ eutectic composition consists of 72 mol% AgCl and 28 mol% CsCl and its eutectic temperature is 258 °C.^[24] AgCl and CsCl powders are mixed at this composition, heated at 470 °C for 2 h, and cooled. **Figure 1a** depicts a scanning electron microscopy (SEM) image of the plan view

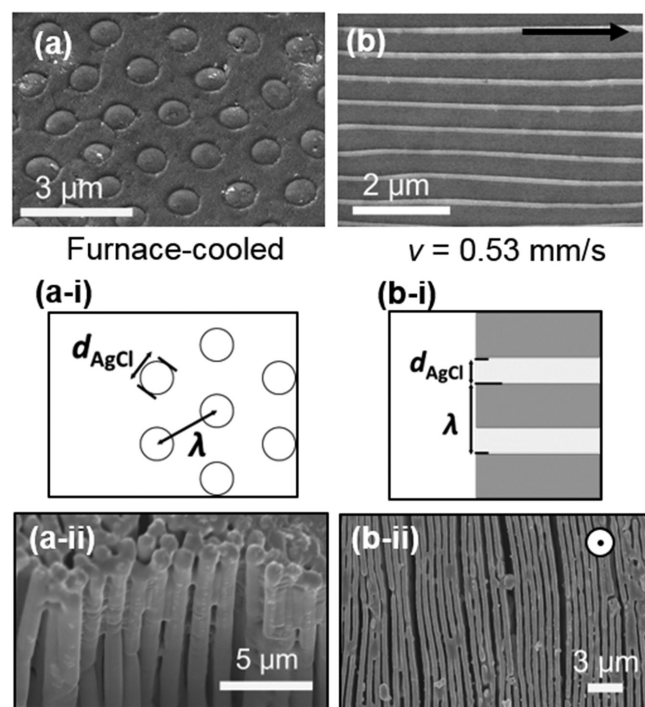


Figure 1. Plan view SEM images of bulk samples showing the microstructures of the a) furnace-cooled rod and b) lamellae solidified with the draw rate of $v = 0.53 \text{ mm s}^{-1}$. Arrow indicates the drawing direction. Corresponding insets show (i) the schematic defining λ and d_{AgCl} in the rod and lamellar structures and (ii) the cross-sectional view SEM images after etching-away CsAgCl₂.

of a bulk furnace-cooled (i.e., effective draw rate $v = 0 \text{ mm s}^{-1}$) AgCl-CsAgCl₂ eutectic sample, showing a structure with rods in a hexagonal lattice arrangement. During furnace cooling, the samples were cooled to room temperature in the furnace (at a rate of about 4 °C min^{-1}) by turning the furnace off. The diameter of the rods (d_{AgCl}) and the rod spacing (λ), as defined in Figure 1a-i, were found to be ≈ 750 and 1490 nm , respectively. Upon selectively etching (see Experimental Section for details), the CsAgCl₂ matrix phase as seen in the cross-sectional view SEM image (Figure 1a-ii), we can discern that the orientation of the rods is perpendicular to the substrate. The fast draw rates (up to $v = 0.63 \text{ mm s}^{-1}$) were accomplished using a syringe pump (see Figure S1a in the Supporting Information) enabling controlled drawing of the molten eutectic samples through the temperature gradient of $\approx 5.1 \text{ °C mm}^{-1}$ in the tube furnace (see Experimental Section for details). Upon directional solidification of the bulk samples with a draw rate of $v = 0.2 \text{ mm s}^{-1}$, the rod diameter and spacing are decreased to ≈ 250 and 440 nm , respectively (see Figure S2 in the Supporting Information). Bulk samples with rod geometry were obtained at draw rates up to $v = 0.2 \text{ mm s}^{-1}$, and d_{AgCl} and λ were observed to decrease with increasing draw rates, as shown in **Figure 2**. For v of 0.27 and 0.33 mm s^{-1} circular rods were seen along with elongated rods or lamellar-like structures (see Figure S2 in the Supporting Information) indicating the formation of a mixed microstructure in this range of draw rates (shaded region in Figure 2). Increasing the draw rates to $v > 0.36 \text{ mm s}^{-1}$, lamellar structures were observed in the bulk structure (see Figure S2 in the Supporting Information). We define d_{AgCl} as the width of the AgCl lamella and λ as the lamellar period (i.e., width of AgCl + width of CsAgCl₂); see Figure 1b-i. The lamellar structure was observed at all higher draw rates, with d_{AgCl} and λ about 115 and 518 nm , respectively at $v = 0.53 \text{ mm s}^{-1}$ (Figure 1b). The lamellae align parallel to the draw direction, as observed in the selectively etched cross-sectional view SEM

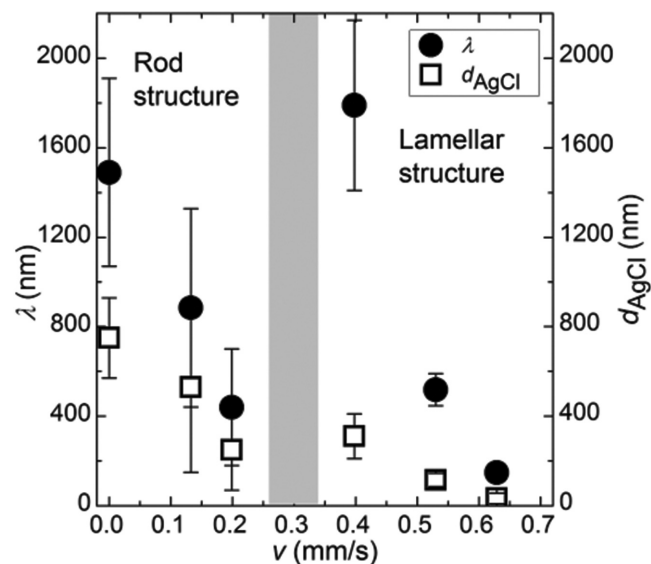


Figure 2. λ and d_{AgCl} plotted as a function of draw rate v . Here, error bars represent ± 2 standard deviations. Shaded region corresponds to the observed mixed structure regime.

image in Figure 1b-ii. When increasing the draw rate from $\nu = 0.4$ to $\nu = 0.63$ mm s⁻¹, the lamellar spacing is decreased from 1790 to 115 nm as shown in Figure 2. Low magnification plan view SEM images (see Figure S3 in the Supporting Information) show the representative rods and lamellar structure domains over 30 $\mu\text{m} \times 30 \mu\text{m}$ area.

The binary phase diagram of the AgCl-CsCl system, shown in Figure 3a, was confirmed by differential scanning calorimetry (DSC) measurements around the eutectic composition. Heat flow curves were measured with DSC for samples with rod and lamellar structures to confirm their melting points at 258 °C (Figure S4a, Supporting Information). Energy-dispersive spectroscopy (EDS) was used to confirm the composition of both the rod-like and lamellar eutectic structures (Figure S4b, Supporting Information). Peaks associated with Cs, Ag, and Cl were observed in the atomic ratio similar to the

expected theoretical ratio of 1:2:3, respectively, for the AgCl-CsAgCl₂ eutectic system. EDS elemental mapping discerns the rod phase as AgCl and the matrix as CsAgCl₂ in the case of the rod geometry (Figure S4c, Supporting Information), and the narrower component as AgCl and the wider component as the CsAgCl₂ phase in the lamellar geometry (Figure S4d, Supporting Information). The composition of the eutectic was further confirmed by X-ray diffraction (XRD), where peaks corresponding to only AgCl and CsAgCl₂ phases were observed for both rod and lamellar structures (Figure 3b).

The low eutectic temperature and low surface energy of the AgCl-CsAgCl₂ eutectic system facilitate infilling of glass tubing (see Experimental Section for details). Using capillary action, borosilicate glass capillaries were infilled with the AgCl-CsAgCl₂ binary eutectic (see Figure S5 in the Supporting Information) and were subsequently cooled either slowly in the furnace (that is allowed to naturally cool) or by drawing out of the furnace (see Figure S1b in the Supporting Information). The former (slow-cooled) capillaries were found to have a hexagonal arrangement of AgCl rods within a CsAgCl₂ matrix (Figure 4a). On the other hand, the capillaries solidified with a draw rate of 0.53 mm s⁻¹ exhibited a lamellar microstructure consisting of alternating layers of AgCl and CsAgCl₂ (Figure 4b). Equal draw rates for both the eutectic-infilled capillaries and the bulk samples yielded similar d_{AgCl} and λ values, regardless of the resulting eutectic morphologies.

Both the rod and lamellar structures are oriented orthogonal to the substrate, with the lamellae aligned along the draw direction. The alignment of the rods relative to the draw direction seems to be counterintuitive because the diffusion near the solidification front (i.e., the solid-liquid interface) parallel to the front is responsible for the simultaneous formation of the two solid phases. However, this alignment can be attributed to the orientation of the solidification direction not coinciding with the draw direction.^[31,37] The orientation of the eutectic solidification front is determined by the details of the heat transfer in the eutectic material and the substrate for the given thermal condition, as previously demonstrated by simulations.^[16,22] Heat transfer simulations were performed using COMSOL to map the temperature profile in the eutectic material during directional solidification (see the Experimental Section for details). For the furnace cooled case, the solidification front (approximated by the eutectic temperature isocontour) is

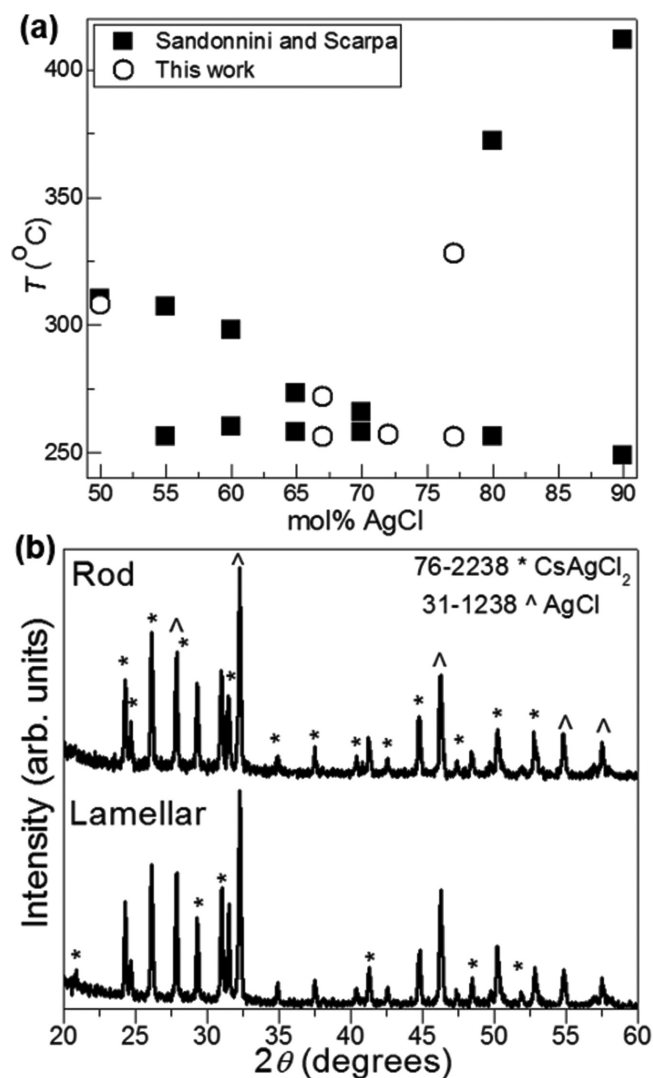


Figure 3. a) Binary phase diagram of AgCl-CsCl system around the eutectic composition compared to the published work of Sandonnini and Scarpa.^[27] b) XRD pattern of rod and lamellar samples showing the constituent AgCl and CsAgCl₂ peaks with no detectable impurity peaks.

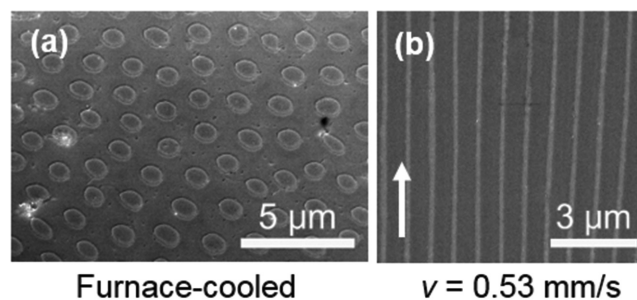


Figure 4. Plan view SEM images of eutectic-infilled capillary showing a) a rod structure for furnace-cooled case and b) a lamellar structure for directionally solidified case at a draw rate of 0.53 mm s⁻¹. Arrow indicates the drawing direction.

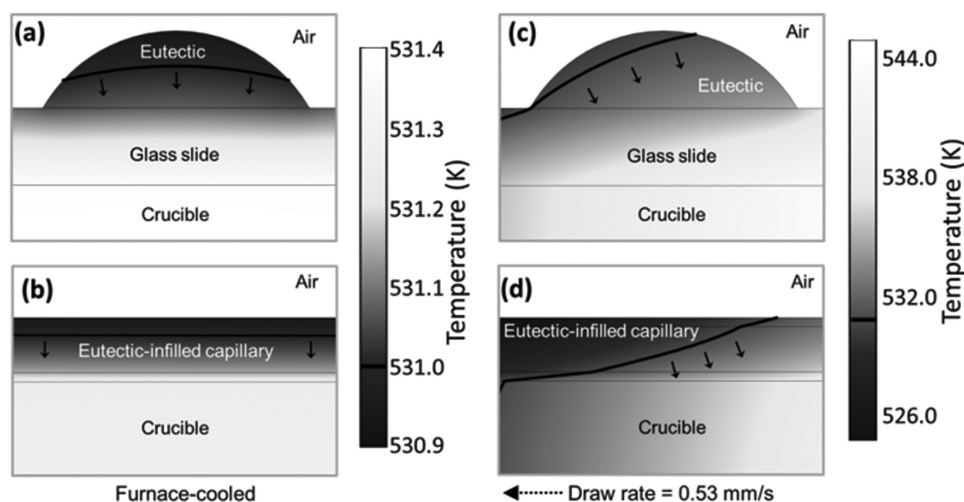


Figure 5. The temperature profiles of the eutectic during solidification for furnace cooling, a) bulk case and b) capillary, and for a draw rate of 0.53 mm s^{-1} c) for bulk case and d) capillary, respectively. Dotted arrow indicates the drawing direction. The temperature in the air is not plotted.

a horizontal plane (shown in **Figure 5a,b**) and indicates a downward solidification direction. For directional solidification with a draw rate of 0.53 mm s^{-1} , the solidification front is inclined at a shallow angle to the top boundary, indicating a solidification velocity with a smaller component in the draw direction and a larger downward component (perpendicular to the draw direction) as shown in **Figure 5c,d**.

Phase-field simulations of eutectic solidification were performed with initial solid structures of rod, lamellar, and mixed configurations as a seed (see **Figure S6** in the Supporting Information) within eutectic liquid; further details can be found in the Experimental Section. For solidification velocities ranging from 0.001 to 5.3 mm s^{-1} , simulations with rods as an initial condition all yielded steady-state structures of rods in a hexagonal arrangement. For the same range of velocities, simulations with mixed or lamellar initial conditions all yielded steady-state structures of ordered lamellae. The steady-state structures are shown in **Figure 6**. The fact that the mixed state converts to the lamellar structures indicates that the lamellar structure is more stable; however, the energy barrier to switch between the rod and lamellar structures must be large enough that the rod phase does not convert to the lamellar phase. Thus, if the rod structure forms initially, then it will persist throughout the sample. Conversely, if a mixed or lamellar structure forms initially, then the lamellar structure dominates.

As discussed earlier, the temperature profiles resulting from fast draw rates calculated by the heat transfer simulations show the solidification front propagating from the top (cooler) boundary toward the hotter boundary beside a small component along the draw direction. Therefore, the initial formation of the eutectic structure would likely occur at the top liquid eutectic–air interface for the bulk samples and the top liquid eutectic–glass capillary interface for the capillary samples. If a compact structure of the minority solid phase is preferred during the initial solidification at the cool boundary, a rod structure would emerge as a result and will persist through the thickness of the sample. These observations suggest that the difference in structures seen in experiments at different

draw rates is likely due to rod structures initially forming at the cool boundary at low draw rates and lamellar structures initially forming at the boundary at high draw rates.

It was possible to vary the directional solidification draw rate for different regions of the same capillary. As an example, **Figure 7a** depicts a eutectic-infilled capillary that was drawn through the tube furnace at $v = 0.53 \text{ mm s}^{-1}$ for about half of its length, with the remaining half being allowed to naturally cool in the furnace. The SEM images at various locations in the capillary show a lamellar region, a lamellar to rod transition region, and a rod region (**Figure 7b**). The lamellar region had $\lambda = 550 \text{ nm}$ and $d_{\text{AgCl}} = 130 \text{ nm}$. This was followed by the lamellar structure transition into rod structure. In this transition region, the

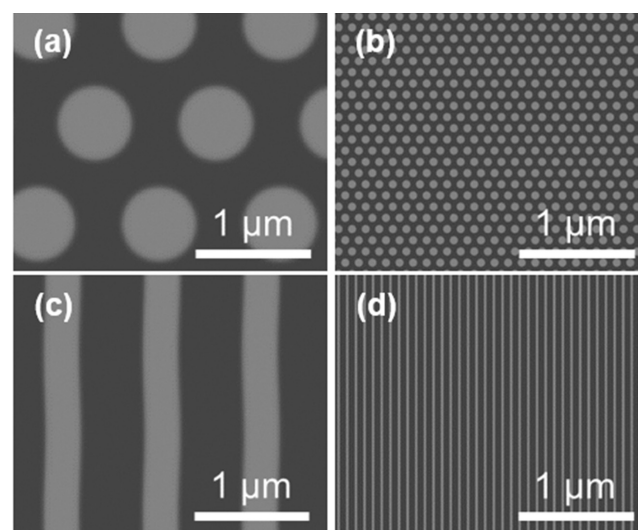


Figure 6. Phase field simulation of directional solidification for a) $v = 0.01 \text{ mm s}^{-1}$ with rod initial condition, b) $v = 0.53 \text{ mm s}^{-1}$ with rod initial condition, c) $v = 0.01 \text{ mm s}^{-1}$ with mixed initial condition, and d) $v = 5.3 \text{ mm s}^{-1}$ with mixed initial condition. Light gray and dark gray represent AgCl and CsAgCl₂, respectively. Images shown consist of the computational domain repeated along periodic boundaries.

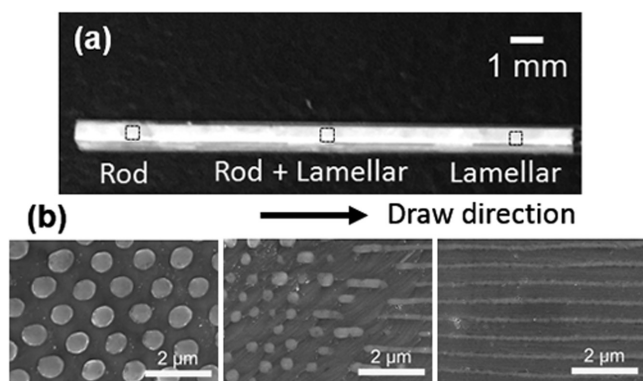


Figure 7. a) Photograph of a eutectic-infilled capillary that was solidified at varying speeds. b) Plan view SEM images from various positions in the above capillary showing the rod structure, the mixed rod and lamellar structure, and the lamellar structure. Arrow indicates the drawing direction.

rods initially had a small diameter and spacing ($\lambda = 440$ nm and $d_{\text{AgCl}} = 250$ nm), likely due to the transience in which the local solidification rate changes from that of fast draw rates to that of natural furnace cooling. As the solidification rate approached the furnace-cooled rate, the rod spacing and diameter increased to steady-state values ($\lambda = 1100$ nm and $d_{\text{AgCl}} = 660$ nm), similar to those observed in the furnace-cooled sample.

Owing to the difference in the refractive indices of the components of the eutectic, these rod and lamellar structures operate as 2D and 1D dielectric photonic crystals, respectively. Normal incidence reflectance spectra were taken from spot sizes of $180 \mu\text{m}$ in diameter from the solidified eutectic-infilled capillaries using a Fourier-transform IR (FTIR) spectrometer microscope, and these reflectance spectra were compared with finite-difference time domain (FDTD) simulations (see Experimental Section for details). **Figure 8a** compares the measured and simulated normal-incidence reflectance spectra of the furnace-cooled sample with a hexagonal array of AgCl rods in CsAgCl₂. The position of the measured reflectance peaks at 1.31 and $1.57 \mu\text{m}$ corresponds to the FDTD-simulated reflectance peak for a model hexagonal photonic crystal of AgCl rods in CsAgCl₂ matrix with $\lambda = 1300$ nm and $d_{\text{AgCl}} = 650$ nm. **Figure 8b** shows the measured and simulated normal-incidence reflectance spectra of a sample drawn at $v = 0.53 \text{ mm s}^{-1}$, which has alternating lamellae of AgCl and CsAgCl₂. For the lamellar structure in the eutectic-infilled capillary, the reflection peaks at 0.97 and $1.95 \mu\text{m}$ agree well with the positions of the reflectance peaks as observed in the FDTD simulations for AgCl-CsAgCl₂ lamellae with $\lambda = 600$ nm and $d_{\text{AgCl}} = 150$ nm. The difference in the peak positions and the broadening of the reflectance peaks could stem from the imperfections in the arrangement and the size of rods or lamellae within a capillary sample, not present in the idealized structure used for simulations. The size distribution in rods and lamellar structure arises from the solidification process as there is always a range of spacing (and size distribution) that lie around the average value close to the minimum undercooling value for a given rate of solidification.^[4,38–40] This distribution in the lattice parameters (as shown in **Figure 2**) may cause the broadening of the reflectance peaks (see **Figure S7** in the Supporting Information). For the samples

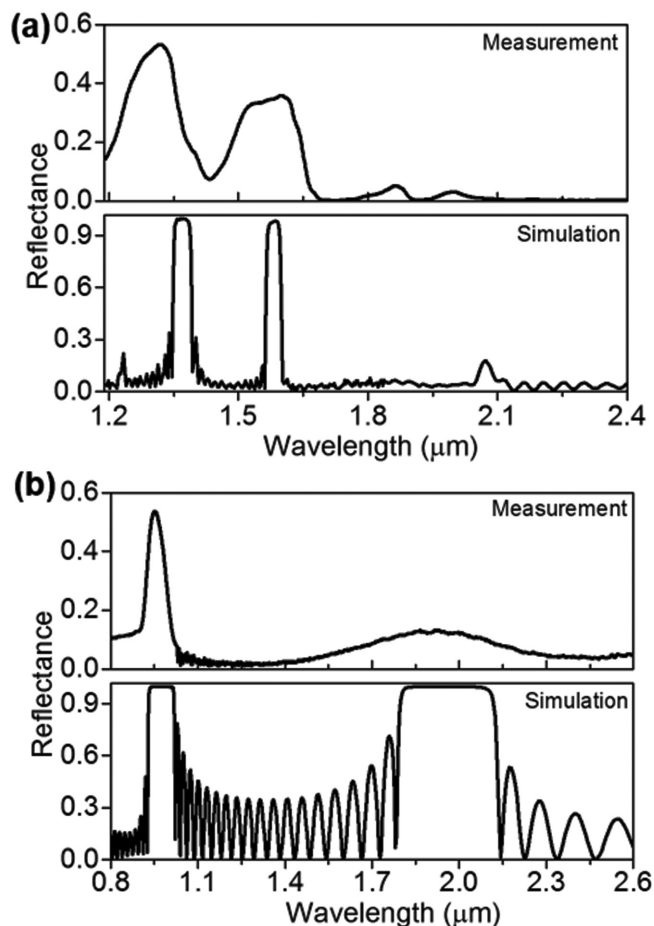


Figure 8. a) Reflectance spectra of the rod structure in a eutectic-infilled capillary measured normal to the rod axis (spot size: $180 \mu\text{m}$ in diameter) and the corresponding FDTD simulation for a hexagonal lattice of AgCl rods (25 layers) with a radius of 325 nm and a periodicity of 1300 nm in CsAgCl₂ matrix. b) Reflectance spectra of the lamellar structure in a eutectic-infilled capillary measured normal to the lamellae (spot size: $180 \mu\text{m}$ in diameter) and the corresponding FDTD simulation for alternating layers (32 layers) of AgCl (150 nm wide) and CsAgCl₂ (450 nm wide). Refractive indices of 2.01 and 1.49 were used for AgCl and CsAgCl₂, respectively, and both materials were treated as lossless.

solidified with varying draw rates, the regular regions (either of rod or lamella) exhibited a similar optical response to the samples drawn at the same constant rate, while the transition region with mixed structures had broad low intensity peaks, which is expected given the low degree of order in this mixed region.

3. Conclusion

In summary, we investigated a rod-to-lamellar microstructure transition in the AgCl-CsAgCl₂ eutectic system driven by the drawing rates during directional solidification through experiments and simulations. The combination of the low melting temperature and a low surface tension of this eutectic in the molten state enables it to easily infill glass tubing, greatly facilitating optical characterization. By varying the drawing rate, not

only the characteristic dimensions of the microstructure but also the lattice symmetry can be controlled. At low solidification rates, the rod structure is present, while at higher solidification rates, the lamellar structure appears. From heat transfer and phase-field simulations, it was established that the solidified structure is strongly influenced by the structure that forms initially at the boundary of the liquid eutectic during solidification, and thus the transition is attributed to the different structure that forms at the cool boundary. Through optical spectroscopy, it was confirmed that the rod and lamellar microstructures of this salt eutectic exhibit the reflectance spectra corresponding to characteristic 2D and 1D photonic crystals, respectively.

4. Experimental Section

Synthesis of Bulk AgCl-CsAgCl₂ Eutectic: As-received high purity AgCl (99.999%, Sigma-Aldrich) and CsCl (99.999%, Sigma-Aldrich) powders were mixed at 41.95 wt% AgCl and 58.05 wt% CsCl, corresponding to the eutectic composition. The powders were then mixed with an agate pestle in an agate mortar at room temperature. The mixed powder was placed in a glass vial and then heated in a tube furnace at 470 °C for 2 h in air, and subsequently cooled to room temperature, with a furnace-cooling rate of about 4 °C min⁻¹.

Directional Solidification Setup: For the directional solidification experiments, a 1" tube furnace (Lindberg Blue M) was heated to 470 °C, and its temperature profile was recorded. The eutectic samples were placed at the mark where the temperature in the furnace tube (1" diameter quartz tube) was at 350 °C (see Figure S1 in the Supporting Information). For bulk samples, the eutectic was melted on a glass slide that was held on an alumina crucible, while the eutectic-infilled capillaries were kept directly on the alumina crucible. This alumina crucible was anchored to a syringe pump (NE-300, New Era Pump Systems Inc.) which enabled drawing the samples through the temperature gradient of ≈5.1 °C mm⁻¹ in the tube furnace, for a distance of ≈120 mm until the samples cooled down to room temperature. With this syringe pump, it was possible to control draw rates (ν) up to 0.63 mm s⁻¹. In the case of furnace cooling ($\nu = 0$ mm s⁻¹), the samples were cooled to room temperature in the furnace, by turning the furnace off. The cooling rate near the eutectic melting temperature was about 4 °C min⁻¹.

CsAgCl₂ Phase Etching: To etch the CsAgCl₂ phase, the bulk samples were immersed in a deionized water bath for 5 s followed by immersion in an ethanol bath for 1 min. The etched bulk samples (etch depth of a few micrometers) were then removed from the bath and air dried with a light stream of N₂.

Fabrication of Eutectic-Infilled Capillaries: 0.2 g of the AgCl-CsCl salt mixture was placed in a 5 mL glass vial and heated in a tube furnace at 470 °C for 2 h in air (see Figure S5 in the Supporting Information). After cooling to room temperature, a borosilicate glass capillary tube was placed in the glass vial. While borosilicate glass tubes of various shapes and size were tested for this work (square, rectangle, or circle), square-miniature hollow glass tubing (VitroTubes) 50 mm in length, with x and y inner dimensions of 0.600 and a 0.120 mm wall thickness were used, as this style of capillary was found to give the most consistent infilling. The vial was heated at 350 °C for 2 h. During this step, the molten eutectic salt was filled 10–30 mm into the glass tube by capillary forces. The molten salt eutectic-infilled capillary was then cooled to room temperature at about 4 °C min⁻¹.

Characterization: SEM images were taken using either Hitachi S-4800 or Hitachi S-4700 SEMs. EDS was collected using an Oxford INCA EDX analyzer, attached to the Hitachi S-4700 SEM. Powder XRD patterns for the rod and lamellar samples were obtained using a Siemens/Bruker D-5000 with Cu K α radiation (1.5418 Å), and XRD patterns from the bulk samples were confirmed using a Philips X'pert MRD system with Cu K α radiation (1.54056 Å). The observed XRD peaks were compared with the database by the Joint Committee on Powder

Diffraction Standards. DSC thermal analysis was carried out using Perkin Elmer Jade Differential Scanning Calorimeter. For DSC analysis, the eutectic samples and CsAgCl₂ powders (≈10 mg) were placed in Pt pans (Perkin Elmer) and covered with Pt lids. Each sample was subjected to three heating and cooling cycles at rates of 10 K min⁻¹. All the DSC measurements were carried out in the temperature range of 180–350 °C. Reflectance spectra were collected from a ≈180 μ m diameter spot on the sample using a Vertex 70 FTIR and a Bruker Hyperion microscope. The borosilicate glass of the eutectic-infilled capillary was removed and the solid eutectic was then polished to a mirror-like surface finish. During optical spectroscopy, these polished samples were oriented such that that incident beam is normal to the rod axis and normal to the alternating lamellar layers. The reflectance spectra across the wavelength range of 0.8 to 1.2 μ m were collected using a 10 \times quartz microscope objective (numerical aperture = 0.25), whereas reflectance spectra across 1.2 to 2.6 μ m were collected using a CaF₂ lens (80 mm focal length and numerical aperture = 0.08). An unpolarized tungsten light source and a CaF₂ beam splitter were used for these measurements. A Si detector was used in the wavelength range of 0.8 to 1.0 μ m, whereas a liquid nitrogen-cooled HgCdTe detector was used in the wavelength range of 1.0 to 2.6 μ m. The change in detector at 1.0 μ m explained the sudden increase in noise around 1.0 μ m in Figure 8b. The reflectance from a silver mirror was used as the reference. The refractive index of CsAgCl₂ was measured using a variable angle spectroscopic ellipsometer (VASE, J.A. Woollam Co. Inc.) over the instrument-limited spectral range of 400–1200 nm and was found to be around $n = 1.49$ with $k = 0$ at 950 nm.

FDTD Simulations: The reflectance spectra from the eutectic microstructures were simulated using the FDTD method with the commercial software FDTD Solutions v.8.16.931, Lumerical Solutions Inc. The FDTD simulations used the SEM-measured d_{AgCl} and λ for the eutectic. Refractive indices of 2.01 and 1.49 were used for AgCl and CsAgCl₂, respectively, and both materials were treated as lossless. For Figure 8a, a hexagonal photonic lattice structure (25 columns of rods in a matrix) was used with a radius of 325 nm and a periodicity of 1300 nm. For Figure 8b, alternating lamellae (32 layers) of 150 nm wide AgCl and 450 nm wide CsAgCl₂ were used. The samples with size distribution (average ± 2 standard deviations) in rods and lamellae were simulated using the values shown in Figure 2. These simulated reflectance peaks (see Figure S7 in the Supporting Information) exhibit the broadened peaks as observed in the reflectance measurements.

Heat Transfer Simulations: The temperature profiles of the eutectic during solidification were simulated in three dimensions using the commercial software COMSOL. Neumann boundary conditions for Newton's law of cooling were applied to all air interfaces with a heat transfer coefficient of 100 W m⁻² K⁻¹.^[41] Air temperatures for the furnace-cooled case were initially 350 °C and decreased at a rate of 4 °C min⁻¹. Air temperatures for the directional solidification case matched those measured in the tube furnace experiment with a moving frame of reference equivalent to the draw rate of 0.53 mm s⁻¹. Temperature profiles for the alumina crucible, glass slide substrate/capillary, and eutectic were calculated as a function of time by solving the heat equation and the solidification front positions were approximated by the isocontour at the eutectic temperature (531 K). The physical constants used to parameterize the heat transfer simulations were assumed to be the same as that of the AgCl-KCl eutectic system,^[16] as K and Cs are Group I elements; other relevant material parameters can be found in Table S1 in the Supporting Information.

Phase-Field Simulations: Eutectic solidification simulations were performed using a phase-field model in which the evolution of the microstructure is described by order parameters. Order parameters represented the phase occupying the point in the system ($P_{\text{CsAgCl}_2}, P_{\text{AgCl}}, P_L$) and are constrained such that their sum is one ($P_{\text{CsAgCl}_2} + P_{\text{AgCl}} + P_L = 1$). In the bulk of the CsAgCl₂ phase, $P_{\text{CsAgCl}_2} = 1$ and $P_{\text{AgCl}} = P_L = 0$. The AgCl and liquid phases are described in a similar manner. At the interfaces between phases, the order parameter values transitioned smoothly between zero and one. The employed phase-field model for eutectic solidification was developed by Folch and Plapp.^[42]

The evolution of the order parameters reduced free energy and is described by an Allen–Cahn equation

$$\tau \frac{\partial p_i}{\partial t} = \nabla^2 p_i + \frac{2}{3} \left[-2p_i(1-p_i)(1-2p_i) + \sum_{j \neq i} p_j(1-p_j)(1-2p_j) \right] + \tilde{\lambda} \sum_j \frac{\partial g_j}{\partial p_i} \Bigg|_{P_{\text{CsAgCl}_2} + P_{\text{AgCl}} + P_i = 1} (\mu A_j - B_j) \quad (1)$$

where τ is the relaxation time, the subscripts i and j indicate the phase (CsAgCl₂, AgCl, liquid), t is the simulation time, $\tilde{\lambda}$ is a coupling constant, g is an interpolation function, and μ is the chemical potential. A and B are a phase's equilibrium concentration and equilibrium chemical free energy, respectively. A_L and B_L are set to zero as only the relative differences between solid and liquid phases are relevant.

The chemical transport of the system is calculated by the diffusion equation written in terms of the chemical potential, μ , which is the first derivative of the free energy with respect to composition and therefore provides the driving force for chemical transport. With an antitrapping current term,^[42] the chemical potential evolution equation is

$$\frac{\partial \mu}{\partial t} = \nabla \cdot (D p_L \nabla \mu) - \sum_i A_i \frac{\partial p_i}{\partial t} + 2a \sum_{i=\text{CsAgCl}_2, \text{AgCl}} (A_i - A_L)(-\hat{n}_L \cdot \hat{n}_i) \nabla \cdot \left(\hat{n}_i \frac{\partial p_i}{\partial t} \right) \quad (2)$$

where D is the diffusion coefficient, $a = 1/(2\sqrt{2})$, and \hat{n} is the unit vector normal to a phase's interface. Further details regarding the physical bases and derivations of the order parameter and chemical potential evolution equations can be found in literature.^[42]

The temperature of each point in the system was calculated based on its distance along the y -direction from the eutectic temperature isotherm plane by assuming a linear thermal gradient (G) in the x -direction (the solidification direction). The y - and z -directions are perpendicular to the solidification direction. The eutectic temperature isotherm had an initial position of x_{int} and moves in the x -direction at the solidification velocity, v . The chemical free energy of each phase changes as a function of temperature during solidification according to

$$B_i = A_i \frac{C(x - vt - x_{\text{int}})}{m_i \Delta C} \quad (3)$$

where m is a phase's liquidus slope. A_i is equal to the scaled equilibrium concentration of phase i and is given by $A_i = (C_i - C_E)/\Delta C$, where C_i is the mole fraction AgCl equilibrium concentration of phase i , C_E is the eutectic concentration, and ΔC is the difference in the equilibrium concentrations of the two solid phases at the eutectic temperature (in the case of AgCl–CsAgCl₂, $\Delta C = 0.5$).

The materials properties used to parameterize the model are found in Table S1 (Supporting Information). The governing equations were discretized with a finite difference scheme with a grid spacing of $\Delta x = 0.8$ in space and a forward Euler time-stepping scheme with a time step of Δt equal to the minimum of $0.1\Delta x^2/D$ and $0.1\Delta x^2\tau_i$ in time. This phase-field model does not account for each phase having a different molar volume; therefore, the eutectic composition is set such that the volume fraction is preserved ($C_E = 68.05\%$ AgCl).

Periodic boundary conditions were imposed on all computational domain boundaries except for those perpendicular to the solidification direction, on which no-flux boundary conditions were imposed. The code was parallelized using domain decomposition utilizing the message passing interface library. The initial undercooling of the solidification front was set according to the Jackson–Hunt theory for a lamellar structure solidifying at the draw rate.^[4] The initial condition for the structure of the solid layer, which served as the seed, was either rods, lamellar, or mixed rods and lamellar (see Figure S6 in the Supporting Information). For the rod initial condition, AgCl cylinders were placed in a CsAgCl₂ matrix in a hexagonal lattice arrangement. The centers of the cylinders were shifted randomly in the y - and z -directions by up

to $\pm 10\%$ of the ideal rod spacing and the radii were adjusted by up to $\pm 10\%$ of the ideal rod radius given by the Jackson–Hunt theory.^[4] For the lamellar initial condition, AgCl lamellae were placed in a CsAgCl₂ matrix with the lamellae aligned along the z -direction. The width (measured in the y -direction) of each lamellar pair was modified randomly by $\pm 10\%$ of the nominal lamellar spacing set by the Jackson–Hunt theory^[4] while conserving the volume. Subsequently, the local width of each AgCl layer was sinusoidally perturbed along the z -direction up to $\pm 10\%$ of the nominal width. The mixed initial condition was a superimposition of the rod and lamellar initial conditions with the AgCl features scaled to preserve the volume fraction. The coldest part of the domain that is entirely solidified was discarded and new liquid was added to the hot side periodically, such that the computational window followed a volume that contained the solidification front. The simulation continued until a steady-state, stable structure was attained.

Supporting Information

Supporting Information is available from the Wiley Online Library or from the author.

Acknowledgements

J.C. and A.A.K. contributed equally to this work. This material is based upon work supported by the Air Force Office of Scientific Research MURI (Multidisciplinary University Research Initiative) FA9550-12-0471. The material presented in this work was carried out in part in the Frederick Seitz Materials Research Laboratory Central Facilities, University of Illinois. E.H. and K.T. acknowledge the computational resources from the Department of Defense High Performance Modernization Program. J.C. would like to thank Jin Gu Kang for help with etching experiments. A.A.K. thanks Julia Kohanek for discussions on DSC measurements, phase diagrams, and eutectic solidification.

Conflict of Interest

The authors declare no conflict of interest.

Keywords

directional solidification, eutectics, microstructure transition, photonic crystals, self-organized

Received: December 4, 2017

Revised: March 7, 2018

Published online: May 7, 2018

- [1] U. Hecht, L. Gránásy, T. Pusztai, B. Böttger, M. Apel, V. Witusiewicz, L. Ratke, J. De Wilde, L. Froyen, D. Camel, B. Drevet, G. Faivre, S. Fries, B. Legendre, S. Rex, *Mater. Sci. Eng. R* **2004**, *46*, 1.
- [2] J. Hunt, K. Jackson, *Trans. Metall. Soc. AIME* **1966**, *236*, 843.
- [3] J. Hunt, K. Jackson, *Trans. Metall. Soc. AIME* **1967**, *239*, 864.
- [4] K. Jackson, J. Hunt, *Trans. Metall. Soc. AIME* **1966**, *236*, 1129.
- [5] J. Llorca, V. Orera, *Prog. Mater. Sci.* **2006**, *51*, 711.
- [6] J. D. Joannopoulos, S. G. Johnson, J. N. Winn, R. D. Meade, *Photonic Crystals: Molding the Flow of Light*, Princeton University Press, NJ, USA **2011**.
- [7] K. A. Arpin, A. Mihi, H. T. Johnson, A. J. Baca, J. A. Rogers, J. A. Lewis, P. V. Braun, *Adv. Mater.* **2010**, *22*, 1084.

- [8] J. D. Joannopoulos, P. R. Villeneuve, S. Fan, *Nature* **1997**, *386*, 143.
- [9] A. Blanco, E. Chomski, S. Grachtchak, M. Ibisate, S. John, S. W. Leonard, C. Lopez, F. Meseguer, H. Miguez, J. P. Mondia, G. A. Ozin, O. Toader, H. M. van Driel, *Nature* **2000**, *405*, 437.
- [10] G. M. Gratson, F. García-Santamaría, V. Lousse, M. Xu, S. Fan, J. A. Lewis, P. V. Braun, *Adv. Mater.* **2006**, *18*, 461.
- [11] R. I. Merino, J. I. Pena, A. Larrea, G. F. de la Fuente, V. M. Orera, *Recent Res. Dev. Mater. Sci.* **2003**, *4*, 1.
- [12] B. A. Parviz, D. Ryan, G. M. Whitesides, *IEEE Trans. Adv. Packaging* **2003**, *26*, 233.
- [13] D. A. Pawlak, G. Lerondel, I. Dmytruk, Y. Kagamitani, S. Durbin, P. Royer, T. Fukuda, *J. Appl. Phys.* **2002**, *91*, 9731.
- [14] Y. A. Vlasov, X.-Z. Bo, J. C. Sturm, D. J. Norris, *Nature* **2001**, *414*, 289.
- [15] M. F. Acosta, S. G. Rodrigo, L. Martín-Moreno, C. Pecharrromán, R. I. Merino, *Adv. Opt. Mater.* **2017**, *5*, 1600670.
- [16] J. W. Boley, K. Chaudhary, T. J. Ober, M. Khorasaninejad, W. T. Chen, E. Hanson, A. Kulkarni, J. Oh, J. Kim, L. K. Aagesen, A. Y. Zhu, F. Capasso, K. Thornton, P. V. Braun, J. A. Lewis, *Adv. Mater.* **2017**, *29*, 1604778.
- [17] K. Fukutani, K. Tanji, T. Motoi, T. Den, *Adv. Mater.* **2004**, *16*, 1456.
- [18] J. Kim, L. K. Aagesen, J. H. Choi, J. Choi, H. S. Kim, J. Liu, C. R. Cho, J. G. Kang, A. Ramazani, K. Thornton, P. V. Braun, *Adv. Mater.* **2015**, *27*, 4551.
- [19] D. A. Pawlak, K. Kolodziejek, S. Turczynski, J. Kisielewski, K. Roźniatowski, R. Diduszko, M. Kaczkan, M. Malinowski, *Chem. Mater.* **2006**, *18*, 2450.
- [20] D. A. Pawlak, S. Turczynski, M. Gajc, K. Kolodziejek, R. Diduszko, K. Roźniatowski, J. Smalc, I. Vendik, *Adv. Funct. Mater.* **2010**, *20*, 1116.
- [21] K. Sadecka, M. Gajc, K. Orlinski, H. B. Surma, A. Klos, I. Jozwik-Biała, K. Sobczak, P. Dłuzewski, J. Toudert, D. A. Pawlak, *Adv. Opt. Mater.* **2015**, *3*, 381.
- [22] Z. Yan, M. Han, Y. Shi, A. Badea, Y. Yang, A. Kulkarni, E. Hanson, M. E. Kandel, X. Wen, F. Zhang, Y. Luo, Q. Lin, H. Zhang, X. Guo, Y. Huang, K. Nan, S. Jia, A. W. Oraham, M. B. Mevis, J. Lim, X. Guo, M. Gao, W. Ryu, J. K. Yu, B. G. Nicolau, A. Petronico, S. S. Rubakhin, J. Lou, P. M. Ajayan, K. Thornton, G. Popescu, D. Fang, J. V. Sweedler, P. V. Braun, H. Zhang, R. G. Nuzzo, Y. Huang, Y. Zhang, J. A. Rogers, *Proc. Natl. Acad. Sci. USA* **2017**, *114*, E9455.
- [23] N. Yasui, Y. Ohashi, T. Kobayashi, T. Den, *Adv. Mater.* **2012**, *24*, 5464.
- [24] N. Yasui, T. Kobayashi, Y. Ohashi, T. Den, *J. Cryst. Growth* **2014**, *399*, 7.
- [25] M. Massaouti, A. Basharin, M. Kafesaki, M. Acosta, R. Merino, V. Orera, E. Economou, C. Soukoulis, S. Tzortzakis, *Opt. Lett.* **2013**, *38*, 1140.
- [26] A. Kiszka, J. Dzielendziak, J. Kazmierczak, in *Eleventh International Symposium on Molten Salts XI*, Proc. Vol. 98 (Eds: P. C. Trulove, H. C. DeLong, G. R. Stafford, S. Deki), The Electrochemical Society, Inc., Pennington, NJ, USA **1998**, p. 398.
- [27] C. Sandonini, G. Scarpa, *Rendiconti Accademia Lincei* **1912**, *21*, 77.
- [28] S. Sternberg, M. Terzi, *J. Chem. Thermodyn.* **1971**, *3*, 259.
- [29] K. N. Street, C. F. St. John, G. Piatti, *J. Inst. Met.* **1967**, *95*, 326.
- [30] J. Livingston, *J. Appl. Phys.* **1970**, *41*, 197.
- [31] R. Racek, G. Lesoult, M. Turpin, *J. Cryst. Growth* **1974**, *22*, 210.
- [32] W. Kurz, B. Lux, *Metall. Mater. Trans. B* **1971**, *2*, 329.
- [33] L. Rátkai, G. I. Tóth, L. Környei, T. Pusztai, L. Gránásky, *J. Mater. Sci.* **2017**, *52*, 5544.
- [34] S. Liu, J. Lee, R. Trivedi, *Acta Mater.* **2011**, *59*, 3102.
- [35] M. Croker, R. Fidler, R. Smith, *Proc. R. Soc. Lond. A* **1973**, *335*, 15.
- [36] A. Parisi, M. Plapp, *Europhys. Lett.* **2010**, *90*, 26010.
- [37] J. Hunt, J. Chilton, *J. Inst. Met.* **1963**, *91*, 338.
- [38] M. Ginibre, S. Akamatsu, G. Faivre, *Phys. Rev. E* **1997**, *56*, 780.
- [39] A. Parisi, M. Plapp, *Acta Mater.* **2008**, *56*, 1348.
- [40] J. Teng, S. Liu, R. Trivedi, *Acta Mater.* **2008**, *56*, 2819.
- [41] X. Hu, A. Jain, K. E. Goodson, presented at *ASME 2005 Summer Heat Transfer Conf. collocated with the ASME 2005 Pacific Rim Technical Conf. and Exhibition on Integration and Packaging of MEMS, NEMS, and Electronic Systems*, San Francisco, California, USA, July **2005**.
- [42] R. Folch, M. Plapp, *Phys. Rev. E* **2005**, *72*, 011602.